Nature Communications

https://doi.org/10.1038/s41467-026-70594-x

Article in Press

Antiferroelectric polarization enabling physical activation in $CuBiP_2Se_6$ for medical image processing

Received: 29 October 2025

Accepted: 26 February 2026

Cite this article as: Lin, Y., Yang, D., Wang, Z. *et al.* Antiferroelectric polarization enabling physical activation in $CuBiP_2Se_6$ for medical image processing. *Nat Commun* (2026). https://doi.org/10.1038/s41467-026-70594-x

Yinan Lin, Dongliang Yang, Zhongyi Wang, Weili Zhen, Tianze Yu, Fei Xue, Hongtao Wei & Linfeng Sun

Antiferroelectric Polarization Enabling Physical Activation in $CuBiP_2Se_6$ for Medical Image Processing

Yinan Lin[1,2], Dongliang Yang[1,2], Zhongyi Wang[3], Weili Zhen [1,2], Tianze Yu[1,2], Fei Xue[3], Hongtao Wei[4], Linfeng Sun[1,2]**

[1]Centre for Quantum Physics, Key Laboratory of Advanced Optoelectronic Quantum Architecture and Measurement (MOE), School of Physics, Beijing Institute of Technology, Beijing 100081, China.

[2]Beijing Key Lab of Nanophotonics & Ultra fine Optoelectronic Systems, School of Physics, Beijing Institute of Technology, Beijing 100081, China.

[3]Center for Quantum Matter, School of Physics, Zhejiang University, Hangzhou 310027, China.

[4]Department of Gastroenterology, Beijing Friendship Hospital, Capital Medical University, National Clinical Research Center for Digestive Disease, No.95 YongAn, Xicheng District, Beijing 100050, China.

Correspondence to: Hongtao Wei, wht001@mail.ccmu.edu.cn.

Correspondence to: Linfeng Sun, sunlinfeng@bit.edu.cn.

Abstract

Antiferroelectric materials, featuring field controllable antipolar ordering and reversible polarization switching, offer a promising platform for hardware efficient neuromorphic computing. The tunable polarization dynamics and layered van der Waals structure enable the multifunctional integration of sensing, learning, and computation within a single device architecture. Here, we demonstrate an antiferroelectric polarization driven diode exhibiting an extended linear operating region, which simultaneously enables physical activation and computing-in-memory. Building on the device capability, we construct an in-sensor computing system that achieves over 95% accuracy in medical image classification. We further integrate the devices to demonstrate a hardware-based activation function, attaining accuracy and training loss comparable to an ideal activation function. To enhance adaptability, we further propose a tunable activation circuit that enables linear modulation of the reverse bias slope via gain control. Overall, this work establishes a dual-functional antiferroelectric heterojunction, highlighting its strong potential for constructing optically triggered, compact, and low-power perception–computation-integrated neuromorphic systems for medical image processing.

Keywords
antiferroelectric dynamics, polarization modulation, physical activation, $CuBiP_2Se_6$

1. Introduction

Against the backdrop of rapid advances in artificial intelligence, deep learning has emerged as a core technology and has been extensively applied across diverse fields, including autonomous driving[1, 2, 3, 4], computer vision[5, 6, 7], and natural language processing[8, 9, 10, 11]. With the continuous evolution of visual models[12, 13, 14], large language models[15, 16], multimodal large language models[17, 18, 19], deep neural networks are reshaping human society at an unprecedented scale and complexity. However, conventional von Neumann architectures[20, 21, 22], which physically separate memory and computation, suffer from increasingly high energy consumption and latency [22, 23, 24]. As indispensable components in deep neural networks,[25] activation functions further exacerbate the burden of data processing and data transfer[26], intensifying the computational and communication overhead between computing and memory units.

Antiferroelectric materials, distinguished by their reversible antipolar ordering and tunable phase transitions, provide a materials-based route toward adaptive computing paradigms. Their field responsive polarization behavior enables efficient in-memory processing, thereby overcoming the inherent data transfer bottlenecks of von Neumann architectures. In contrast to conventional ferroelectrics, antiferroelectric materials exhibit reversible and energy-efficient polarization switching, supporting repeatedly executable analog computing operations[27, 28]. These properties naturally map onto the continuous and plastic behaviors required for synaptic weight modulation in neuromorphic systems. Moreover, their layered van der Waals structure facilitates scalable integration with 2D semiconductors, enabling the synergistic realization of sensory perception, synaptic plasticity, and in-memory computing within a unified device framework. Most current implementations of activation functions still rely on external processors for computation[29] or CMOS-based activation functions. This decoupling not only increases system complexity but also limits the potential for monolithic, compact, and energy-efficient neuromorphic platforms. This leads to high interconnect energy consumption and necessitates large area analog to digital converters, posing major challenges for hardware efficiency in edge computing systems[30, 31]. Therefore, achieving seamless integration of activation functionality within memristive devices is a potential solution. In addition to activation function integration, another critical challenge in in-sensor computing lies in maintaining high signal fidelity during large scale data processing, particularly in noisy or resource constrained edge environments. Ultraviolet (UV) light, with its inherently high signal to noise (SNR) ratio, is particularly advantageous for maintaining signal fidelity under such demanding conditions[32], which is of paramount importance for ensuring reliable feature extraction and diagnostic accuracy in medical image processing applications addressed in this work. Although few studies have attempted to implement activation functions using CMOS based circuits or hybrid materials[33, 34], These solutions often suffer from increased circuit complexity, limited scalability, and incompatibility with emerging material platforms. However, the lack of seamless integration[35, 36] between activation and sensing components, prevents true in-situ data processing, thereby undermining the potential of monolithic neuromorphic architectures.

In this study, we present an antiferroelectric heterojunction integrating $CuBiP_2Se_6$ (CBPS) and MoS_2 that unifies sensing, computation, and activation. The device exhibits an extended linear operating region under forward bias driven by antiferroelectric polarization, together with a finite reverse-bias slope ($\alpha \approx 0.02$), resulting in a nonlinear transfer characteristic. This nonlinear mapping, intrinsically generated by the device physics and resembling the commonly used activation functions in neural networks, is defined as physical activation. Under UV stimulation, the heterojunction exhibits synaptic characteristics, enabling its direct implementation in an in-sensor computing architecture where it simultaneously

functions as a reservoir and a nonlinear activation unit. This enables an energy-efficient perception–computation pipeline for three dimensional medical image classification, achieving an accuracy over 95%. We further integrate the device into a vision transformer as a physical activation function, attaining accuracy comparable to the ideal activation function while reducing training loss during backpropagation. The designed antiferroelectric polarization enabling physical activation for tunable activation circuit offers task adaptive, circuit level configurability for neuromorphic network design.

2. Results and discussion

2.1. Antiferroelectric Heterojunction Characterization and Electrical Volatile Switching Behavior

To realize a dual functional device, two key criteria must be satisfied, volatile behavior with diode like rectification under electrical stimulation, and synaptic behavior under optical stimulation. CBPS, a two dimensional antiferroelectric material, exhibits rapid polarization recovery and abrupt current switching under bias, making it suitable for fast and volatile electrical operation. In contrast, MoS_2 is a well established 2D semiconductor with excellent photoresponse, capable of generating strong and persistent photocurrents. When integrated into a heterostructure, the resulting CBPS/MoS_2 device exhibits both rapid electrical recovery and prominent optically induced synaptic characteristics, such as light triggered synaptic potentiation and short-term memory behavior. This enables the seamless integration of nonlinear electrical activation and optoelectronic synaptic responses within a single device. Figure 1 illustrates the design of this dual functional heterojunction device, which supports both in-sensor computing and neuron activation, serving as a key element for low-power and highly integrated neuromorphic systems. Convolutional neural networks require nonlinear activation functions following convolution and weighted summation operations to enhance feature extraction and model expressiveness. However, in conventional architectures, activation functions are typically computed by separate processors, leading to frequent data transfer between sensing and computing units. This results in increased energy consumption and latency, posing a major bottleneck for in-sensor computing systems. Figure 1a presents the envisioned application of the CBPS/MoS_2 heterojunction device within a neural network framework. The device can directly sense optical input and generate photocurrent responses, enabling integrated "sense compute" functionality. Simultaneously, its asymmetric I–V characteristics emulate a LeakyReLU activation function, allowing the device to replace traditional processor based activation units and act as a hardware level physical activation function. An optical micrograph of the fabricated device and a 1×5 array are provided in Figure S1 and S2 (see Supporting Information), showing the heterojunction layout on a SiO_2/p++ Si substrate (with 300 nm SiO_2). To further confirm the thickness of the CBPS/MoS_2 heterostructure, atomic force microscopy (AFM) is performed to examine the topography and profile of the device, as shown in Figure S3. The height profile measured along the path indicated in the inset reveals that the MoS_2 flake has a thickness of approximately 3.8 nm, while the CBPS layer measures around 13.4 nm. The optical absorption of MoS_2 and CBPS is low at small thicknesses and saturates as thickness increases[37, 38]. Consequently, a moderate thickness is preferred to balance the requirements for high mobility and sufficient absorption. The room temperature polarization-electric hysteresis loop (P-E loop) of CBPS is measured to confirm its antiferroelectric behavior, as presented in Figure 1b. It is observed that an external electric field induces a polarized state in CBPS (also referred to as field induced ferroelectric state). As shown in Figure 1b, when the electric field returns to zero, the remanent polarization is −0.86 μC/cm², indicating that the polarization is close to zero, which is consistent with the spontaneous depolarization behavior characteristic of antiferroelectric materials. By extracting the first derivative of the P-E loop (Figure S4), a pronounced discontinuity is observed at approximately 50 kV cm^{-1}, indicating a rapid polarization switching process occurring at this field. To quantitatively evaluate

the loop symmetry, we extract two parameters. The polarization values at +200 kV/cm and −200 kV/cm are +9 μC/cm² and −9 μC/cm², respectively. In addition, the loop areas obtained during forward and reverse scans are 171.04 and 138.36, respectively. We measure the P-E loop hysteresis loops of CBPS at various thicknesses (Figure S5). The loops consistently exhibit antiferroelectric characteristics across all measured thicknesses. To investigate the polarization direction, we perform piezoresponse force microscopy (PFM) measurements. The cyclic PFM amplitude and phase images obtained from multiple cycle PFM measurements with continuous voltage scanning, as shown in Figure S6, reveal significant domain evolution. During a +4 V voltage scan, a clear phase shift appears, indicating the occurrence of domain switching. Transmission electron microscopy (TEM) and energy dispersive spectrometry (EDS) are employed to confirm a clean interface and homogenous elemental distribution of the device. TEM images demonstrate that our fabricated vdW heterojunction has clean interfaces between the 2D materials. Raman spectroscopy is employed to identify the constituent van der Waals (vdW) nanoflakes, as shown in Figure S7. The Raman spectrum of CBPS exhibits five characteristic peaks located at 111.7 cm^{-1} (E^1_g), 135.3 cm^{-1} (E^2_g), 207.5 cm^{-1} (A^1_g), 431.9 cm^{-1} (A^2_g), and 465.9 cm^{-1} (A^3_g), which are consistent with previous reports[38]. Additionally, the frequency difference of 24.5 cm^{-1} between the E^1_{2g} (383.3 cm^{-1}) and A_{1g} (407.8 cm^{-1}) modes confirms the multilayer structure of MoS_2[39]. A detailed schematic of the device structure employed in Figure 1a is presented in Figure 2a. The device consists of vertically stacked p-type antiferroelectric CBPS and n-type two dimensional semiconductor MoS_2, with an in plane electrode configuration. Under DC voltage sweeps from –3 V to 3 V (Figure 1d), the device exhibits a pronounced asymmetric current–voltage (I–V) response, with a sharp increase in current observed under forward bias, while conduction under reverse bias is suppressed. This behavior closely resembles the LeakyReLU activation function, indicating the device's suitability for hardware level nonlinear activation in neural networks. The inset in Figure 1d presents the linear fitting of the DC I–V curves in both the forward and reverse regions, revealing high linearity. The piecewise-linear function (PWLF) method was employed for the fitting (see Supplementary Note 1). The calculated coefficient of determination (R^2) is 0.999, with a normalized root mean square error (NRMSE) of 0.0098, which demonstrates a high degree of linearity. Figures 1e presents the mechanism of the heterostructure under voltage sweeping. The nonlinear behavior arises from the combined action of the built-in electric field and the ferroelectric polarization, which are formed at the interface between n-type MoS_2 and p-type CBPS. In the unbiased state, the dipoles within CBPS are oppositely oriented, leading to mutual cancellation of the overall polarization and thus exhibiting a neutral polarization state. When a forward bias is applied, the external electric field partially compensates the CBPS/MoS_2 built-in field and drives the dipoles to realign along the field direction, resulting in a polarization orientation inside the material. During the reverse voltage sweep, the relaxor antiferroelectric nature of CBPS induces an ordered polarization state, resulting in high conductance. As the voltage is withdrawn, the remnant polarization field rapidly dissipates, accompanied by rapid restoration of antiferroelectric domains, leading to a narrow and volatile memory window under forward bias. In contrast, under reverse bias, the built-in electric field aligns with the external field at the heterointerface impedes Cu-ion migration in CBPS, suppressing the formation of ordered polarization states and consequently erasing the memory notch. This unique volatile behavior exhibited by the heterostructure is particularly suitable for iterative computing applications.

Figure 2 illustrates the nonlinear and volatile electrical conductance behavior of the CBPS/MoS_2 heterojunction device under electrical stimulation, highlighting its potential as a physical activation function. Bidirectional DC voltage sweeps (-3 V to +3 V to -3 V) at different sweeping rates are further performed, as illustrated in the inset of Figure 2b. The results show negligible conductance hysteresis in the reverse sweep, indicating a near zero memory window, while only a very small memory window is observed in the forward direction. These findings confirm the highly volatile nature of the device. Moreover, the memory window of the device shows negligible dependence on the scan rate. Figures 2c

to 2f further investigate the device's conductance dynamics under pulsed electrical stimuli. Figures 2c and 2d demonstrate that, under varying pulse amplitudes (with a fixed pulse width of 100 ms) and varying pulse widths (at a constant 5 V amplitude), the device exhibits a rapid increase in current that quickly saturates, with a read voltage fixed at 0.1 V. The extracted current responses at different pulse amplitudes (inset in Figure 2c) show a consistent linear dependence on the applied voltage, indicating stable and predictable electrical behavior. According to the Shockley diode equation (see Supplementary Note 2), the current exhibits an exponential increase as the applied voltage gradually raised. However, the extracted linear response demonstrates that in CBPS, the polarization-induced electric field counteracts the applied electric field, resulting in a highly linear process with a NRMSE of 0.0722. Subsequently, we tested the device's response to successive pulsed stimuli. Figure 2e, 2f and S8 show the current response under 1 to 20 electrical pulses with amplitudes of ±3 V and ±5 V. The current reaches a steady state after approximately five pulses and remains stable thereafter, demonstrating the device's robustness and reliability as a physical activation unit. Inset of Figure 2e shows a magnified view of the region highlighted in red, where the channel conductance trend clearly stabilizes. To evaluate the cycling stability and device uniformity, the cycle-to-cycle and device-to-device variability are presented in Figure S9. The devices exhibit quantitatively similar responses, indicating good uniformity, with a cycle-to-cycle mean standard deviation (STD) of 0.014 and a device-to-device mean STD of 0.023. We apply an electrical pulse with a width of 500 µs and amplitude of 1 V to estimate the energy consumption, yielding an energy consumption per computation event of 95.5 pJ (Figure S10a). We compare the computation time and power consumption of CBPS/MoS_2 with other device based activation functions in Table S1. The results demonstrate that the proposed device achieves superior energy efficiency. Figures 2g and 2h schematically depict the band alignments before and after the formation of the CBPS/MoS_2 heterojunction. Specifically, the work function of MoS_2 is approximately 4.5 eV with an electron affinity of ~4.0 eV and a bandgap of ~1.3 eV[40, 41], while CBPS exhibits a larger work function of ~5.26 eV and a bandgap of ~1.27 eV[38]. A type-II band alignment is established, with the built-in electric field oriented from CBPS to MoS_2. This built-in field, in combination with an external bias, modulates the depletion region width, thereby controlling the turn on and turn off states of the channel, which explains the observed asymmetric I–V characteristics and supports the emulation of an activation function like behavior. Under forward bias (Figure 2i), the depletion width narrows and the diffusion current increases, further enhancing the device's forward conduction. The CBPS/MoS_2 heterojunction exhibits asymmetric I–V characteristics, making it a promising candidate for use as a physical activation function in neuromorphic computing systems, particularly in compact, low-power, in-sensor computing neural nodes.

2.2. Optoelectronic Synaptic Plasticity in CBPS/MoS_2 Heterojunction Devices

To evaluate the potential of the device as a photonic synaptic element for optical in-sensor computing architectures, Figure 3 presents the synaptic behavior of the CBPS/MoS_2 heterojunction device under laser illumination. As shown in Figure 3a, the device generates a photocurrent response upon exposure to pulsed light (365 nm). Figure 3b shows a typical EPSC response to a single 500 ms light pulse (with a constant forward bias of 0.1 V). After the pulse terminates, the current gradually decays, demonstrating short-term plasticity (STP) akin to biological synapses. Figure 3c further investigates the EPSC amplitudes under various power densities. The EPSC amplitude increases with light intensity, indicating high sensitivity to the illumination strength. Figure 3d explores the influence of pulse width (ranging from 1 ms to 50 ms) on EPSC amplitude, showing that longer pulses induce stronger synaptic responses. We employed a 1 ms pulse to estimate the computational energy consumption (Figure S10b). The resulting energy per computation is estimated to be approximately 3.6 pJ. Subsequently, we varied the number of light pulses to evaluate multi pulse responses. Upon applying 5, 10, 20, and 100 stimulation pulses, the

corresponding relaxation behaviors were recorded, as shown in Figure S11a. The relaxation time is extracted and fitted using the stretched-exponential function[42], which is expressed as,

$$\phi(t) = I_0 * e^{-(t/\tau)^{\beta}} \quad (1)$$

Here, $\phi(t)$ is the relaxation function, τ is the characteristic relaxation time, I_0 is the prefactor, and β is the stretch index ranging between 0 and 1. The obtained fitting results are summarized in Figure S12. After a single pulse, the extracted τ is approximately 1 s, indicative of STP. With increasing pulse number, τ increases and reaches nearly 1 minutes at 100 pulses, demonstrating a transition from STP to long-term plasticity (LTP) under repeated stimulation. In Figure S11b, application of 100 successive light pulses leads to a gradual increase in device conductance, confirming the emergence of long-term memory behavior. Figures 3e and 3f validate the self-driven operation of the device under zero bias. Responses are recorded under varying power densities (ranging from 3 mW/cm^2 to 15 mW/cm^2, Figure 3e) and pulse widths (ranging from 2 ms to 1 s, Figure 3f), confirming stable self-driven current without external bias. The extracted current responses under different UV power densities are plotted in Figure 3g, and fitting to the power-law relation $I \sim kP^{\alpha}$ yields an exponent of $\alpha \approx 0.935$ (NRMSE = 0.014), further confirming a highly linear photocurrent response to power density and indicating drift dominated current transport[43]. To further assess stability, we applied 10 consecutive light pulses, and as shown in Figure S13, the device exhibits consistent photocurrent responses across all pulses, reinforcing its reliability in self-driven mode. Figures 3h and 3i illustrate the carrier transport mechanism of the device under optical illumination. Incident photons are absorbed by the MoS_2 layer, generating electron–hole pairs. These photogenerated carriers are then separated and transported under the combined influence of the built-in electric field at the heterojunction interface and any applied external bias, resulting in a measurable photocurrent. Under forward bias conditions (Figure 3i), carrier injection is enhanced, leading to an increased photoresponse. Even under zero or weak bias (Figure 3h), the built-in field is sufficient to drive carrier separation and transport, enabling self-driven operation through the photovoltaic effect. We also performed a paired pulse facilitation (PPF) test to quantify the short-term synaptic enhancement behavior. As shown in Figure S14a, two consecutive light pulses with a time interval Δt (under a constant bias of –0.1 V) are applied. The second pulse induces a larger EPSC (ΔA_2) compared to the first (ΔA_1), confirming the presence of typical PPF behavior. The PPF index is calculated using the formula $PPF = \Delta A_2 / \Delta A_1 \times 100\%$, quantifying the facilitation effect. The dependence of the PPF index on Δt is summarized in Figure S14b. The data are well fitted using a double exponential decay model,

$$PPF = C_0 + C_1 e^{-\Delta t/\tau_1} + C_2 e^{-\Delta t/\tau_2} \quad (2)$$

Here, the time constants τ_1 and τ_2 correspond to different temporal scales of decay, reflecting the device's ability to respond across multiple memory timescales. The pronounced synaptic responses observed under optical stimulation indicate that the CBPS/MoS_2 heterojunction device holds strong potential as an optoelectronic synaptic node for integration into in-sensor computing architectures.

2.3. In-Sensor Computing Based on the Dual Functional Device

Employing the dual functional properties of the CBPS/MoS_2 heterojunction device, we experimentally implemented a 4 × 5 letter image recognition task, as illustrated in Supplementary Note 3 and Figure S15. Experimental results demonstrate close agreement with simulation in weight programming, network outputs, and final classification tasks, validating the CBPS/MoS_2-based in-sensor system reliably accomplishes the intended letter recognition tasks. To further extend this validation to a more complex and practical task, we constructed an in-sensor computing system simulation for three-dimensional medical image classification. The overall architecture and performance evaluation of the system are presented in Figure 4. As shown in Figure 4a, the OrganMNIST3D dataset[44] is used as the input, which contains 3D CT images of multiple organs and serves as time sequence data. In this study, five organ

categories are selected, including liver, heart, left lung, right lung, and spleen (the specific 3D image categories are presented in the Supplementary Video 1). Each 3D image consists of 64 frames with a resolution of 64 × 64 pixels per frame. Each image is fed into the reservoir frame by frame, and features are extracted every four time steps to generate the corresponding feature maps. Figure 4b illustrates the core architecture of the neural network. The 3D image sequence are transformed into a temporal evolution vector, which is then processed by the reservoir acting as the perception unit. The output signals from the reservoir are sampled and fed into a readout layer for classification. In this architecture, the CBPS/MoS_2 device functions as a physical activation function in the readout stage, utilizing its nonlinear I–V characteristics to perform hardware level activation, thereby enabling a fully integrated data flow from acquisition to computation and decision. To visualize the separability of the extracted features, linear discriminant analysis (LDA) is employed to reduce the dimensionality of the reservoir output. As shown in Figure 4c, the resulting 2D projections of the feature points form clearly separable clusters corresponding to different organ classes, indicating the strong discriminative capability of CBPS/MoS_2 based reservoir. Figure 4d shows the test accuracy over training epochs. After approximately 20 epochs, the test accuracy rapidly increases and stabilizes above 95%, while the training loss continues to decrease. This demonstrates that the neuromorphic computing system based on the dual functional device is capable of efficient feature extraction and classification for complex spatiotemporal image sequences. Figure 4e presents the confusion matrix of the classification results, showing that the recognition accuracy for organs such as the liver, heart, lung, and spleen exceeds 97%, with some categories approaching 100%, further validating the robustness and reliability of the proposed system.

2.4. Generalization Capability of the CBPS/MoS_2 Based Activation Function and Circuit Design

To further evaluate the generalizability of the proposed CBPS/MoS_2 heterojunction device as a physical activation function, we embedded it into mainstream neural network architectures by replacing the conventional LeakyReLU function in image classification tasks. As shown in Figure S16, the CBPS/MoS_2 based activation function is integrated into the multilayer perceptron (MLP) modules of the vision transformer architecture, forming a “physical activation layer”. Input images are divided into patches, embedded with positional encodings, and processed through the transformer encoder. Then, the CBPS/MoS_2 device is used to emulate the LeakyReLU activation behavior. Figure S17 shows examples of the eight class BloodMNIST dataset[44] used for training, including the following cell types, basophil, eosinophil, erythroblast, immature granulocytes (myelocytes, metamyelocytes and promyelocytes), lymphocyte, monocyte, neutrophil, and platelet (arranged from top-left to bottom-right). Figures 4f and 4g compare the test accuracy and training loss curves obtained using the CBPS/MoS_2 activation function versus the ideal LeakyReLU. In both cases, the models achieved nearly identical convergence rates and final loss values, demonstrating the functional equivalence and training stability of the device based activation function. The classification results are summarized in the confusion matrix shown in Supplementary Figure S18, where diagonal elements represent correct predictions and other elements indicate misclassifications. Figure 4h presents saliency heatmaps of Figure S17 obtained using the Grad-CAM++ method[45], which visualizes the regions on which the model focuses during prediction (see Supplementary Note 4). As shown, the model incorporating the CBPS/MoS_2 activation function effectively concentrates on discriminative cellular features, indicating preserved semantic attention capability. To further validate cross task generalization, we applied the CBPS/MoS_2 activation function in vision transformer models trained on multiple diverse datasets, including CIFAR10[46], Oxford-IIIT Pets[47], and Food101[48] (Figure S19a), as well as across various neural network architectures (LeNet[49] and fully connected ANN) trained on the same dataset (MNIST, Figure S19b). We summarize the training loss and accuracy of different models and datasets using both the device based activation function and the

ideal LeakyReLU in Table S2. The results demonstrate that the device physics-based activation function proposed in this work can closely approximate the performance of the ideal activation function. The detailed architectures of LeNet and the ANN are shown in Figure S20. In all cases, the CBPS/MoS_2 activation function achieved consistently high accuracy and enabled effective loss minimization during backpropagation, confirming its strong nonlinear expressiveness and adaptability across diverse networks and tasks. To account for the impact of device variability, the Gaussian noise with different STD is introduced after the activation in each model, and its effect on classification performance is investigated (Figure S21). Classification accuracy remains robust against an increasing STD values up to 0.1, with no observable performance drop. Since the maximum standard deviation of the experimentally measured cycle-to-cycle variability in this device is only 0.018, we conclude that the intrinsic device variability has a negligible impact on classification accuracy in the demonstrated tasks.

To further enhance the generalizability and task adaptability of the device based activation function, we designed a tunable activation circuit capable of adjusting the negative slope of the response curve. Simulations are conducted using the LTspice platform, and the results are shown in Figure S22-S26. As illustrated in Figure S22, the circuit incorporates a nonlinear activation unit based on the CBPS/MoS_2 heterojunction device as the input element. A multistage operational amplifier structure is employed to form a variable gain path. Under negative input conditions, the circuit allows modulation of the response slope in the negative region by adjusting the feedback resistor network (R_5 and R_6), which controls the overall gain factor (Av). By comparing a reference voltage (V_{ref}) with the input voltage (V_{in}), a multiplexer is used to select the appropriate output signal, enabling compatibility with neural networks that require different levels of nonlinear sensitivity to negative inputs. To better illustrate the working principle of the tunable activation circuit, Figure S23 presents a logic flow diagram that outlines the signal selection process. The input voltage V_{in} is continuously compared with a reference voltage V_{ref}. When $V_{in} > V_{ref}$, the circuit enables the default amplification path with a unit slope (slope = 1). Otherwise, a reduced amplification path is activated, and the output follows a weaker slope (α) tunable through the gain configuration. This decision making mechanism is implemented via the analog multiplexer controlled by the enable signal V_{en}. Figure S24 shows the simulated voltage transfer curve of the circuit, highlighting the coordination between the input voltage, the enable signal V_{en} (magenta), and the output voltage V_{out} (orange). As the input voltage rises and crosses the threshold defined by V_{ref}, V_{en} switches from low to high. This transition triggers the multiplexer to select between the two output branches, thereby controlling the slope of V_{out}. In the weaker slope region, a shallow output slope α is maintained, while in the positive input region, a unit slope amplification is activated. This selective response demonstrates how the circuit achieves programmable, asymmetric activation characteristics. Figure S25 presents simulated I–V curves of the activation circuit under various gain settings (Av = 0.1–1.75). While the forward bias region maintains the original activation characteristics of the device, the slope of the reverse bias region increases linearly with Av, demonstrating continuous and controllable slope tuning. Figure S26 further analyzes and fits the relationship between the slope coefficient (α) and the gain factor (Av), confirming a well defined linear correlation.

3. Discussion

In this study, we propose and validate a multifunctional neuromorphic device based on a CBPS/MoS_2 heterojunction, integrating electrical activation and optical synaptic properties. The device exhibits asymmetric nonlinear transfer characteristics analogous to neural network activation function, eliminating the need for external processors. Considering the high SNR required for medical image processing, the device is stimulated with UV illumination to leverage its photonic synaptic functionality. Under UV illumination, the device demonstrates biologically inspired synaptic behaviors, enabling adaptive UV

sensing and supporting medical image processing. Leveraging these properties, the device is embedded into an in-sensor computing architecture and applied to image classification, achieving efficient spatiotemporal feature extraction and recognition. Moreover, its activation function is incorporated into deep learning models, showing comparable performance to ideal nonlinear activation function across datasets. To enhance versatility, a tunable activation circuit is simulated, allowing linear control of the activation slope. A comparison of key metrics (device structure, neural network application, switching energy, and classification accuracy) among leading antiferroelectric materials for neuromorphic computing underscores our contribution, as summarized in Table S3. Our approach not only ensures low power consumption but also achieves a dual-functional device that integrates electrical activation and optical synaptic behavior. Overall, this work establishes a scalable pathway toward compact, hardware adaptive edge systems for medical image processing.

4. Methods

Heterostructure Preparation and Device Fabrication

Atomically thin $CuBiP_2Se_6$ and MoS_2 are mechanically exfoliated from bulk crystals and transferred to a silicon substrate with a 300 nm thick SiO_2 layer via the dry transfer method using polydimethylsiloxane (PDMS). Subsequently, the device is coated with polymethyl methacrylate (PMMA 950 A4) by spin-coating, with an initial speed of 500 rpm for the first 10 s, followed by 4000 rpm for 60 s. After baking the sample on a hot plate at 180 °C for 2 min, electron beam lithography (EBL) is used to develop and fix the electrode patterns for the source and drain. Finally, 5 nm/50 nm Cr/Au electrodes are deposited using thermal evaporation, and acetone is used to remove the unexposed PMMA and excess metal.

Device Characterizations

The electrical behavior of the device under various optoelectronic pulse conditions is investigated using a Keithley B1500A semiconductor parameter analyzer and a Lakeshore CRX-VF probe station. The optical microscope image of the device is captured with an optical microscope, and the height profile of the 2D thin films within the heterostructures is characterized using atomic force microscopy (AFM). Raman spectra are recorded with a confocal Raman spectrometer, employing an excitation wavelength of 532 nm. The ferroelectric measurement was performed by ferroelectric analyzer (Huace FE-2000 Analyzer) in a probe station (CRX-6.5, LakeShore).

Simulation of the In-Sensor Computing System with the CBPS/MoS_2 heterojunction

Firstly, the heterojunction serves as the reservoir mode in simulated in-sensor computing system. The readout layer consists of a two layer multilayer perceptron (MLP) with 500 hidden neurons, where the heterojunction device is employed as the activation function following the first linear layer. The learning is carried out by minimizing the categorical cross entropy loss using a minibatch (batch size = 8) gradient descent with the Stochastic Gradient Descent (SGD) optimizer (initial learning rate = 0.001, momentum = 0.9, weight decay = 5×10^{-5}, the learning rate is multiplied by a factor of 0.95 every 10 epochs).

Simulation of the Vision Transformer with the CBPS/MoS_2 heterojunction

The vision transformer model used in this task is ViT-B/16, which refers to the “Base” variant with 16 × 16 input patch size. During training, the pretrained weights of ViT-Base-Patch-224-in21k are first loaded. These weights are pretrained on the ImageNet-21k dataset, enabling improved model performance. the learning is carried out by minimizing the categorical cross-entropy loss using a minibatch (batch size = 8) gradient descent with the Stochastic Gradient Descent (SGD) optimizer (initial learning rate = 0.001,

momentum = 0.9, weight decay = 1×10^{-4}, the learning rate is multiplied by a factor of 0.9 every 20 epochs).

5. Data availability

The data that support the findings of this study are available from the corresponding author upon reasonable request.

6. Code availability

The codes that support the findings of this study are available from the corresponding author upon reasonable request.

References

1. Guan Y*, et al.* World Models for Autonomous Driving: An Initial Survey. *IEEE Transactions on Intelligent Vehicles*, 1-17 (2024).

2. Ha T*, et al.* AI-driven robotic chemist for autonomous synthesis of organic molecules. *Science Advances* **9**, eadj0461 (2023).

3. Xu Z*, et al.* DriveGPT4: Interpretable End-to-End Autonomous Driving Via Large Language Model. *IEEE Robotics and Automation Letters* **9**, 8186-8193 (2024).

4. Zhou X*, et al.* Vision Language Models in Autonomous Driving: A Survey and Outlook. *IEEE Transactions on Intelligent Vehicles*, 1-20 (2024).

5. Zhao X, Wang L, Zhang Y, Han X, Deveci M, Parmar M. A review of convolutional neural networks in computer vision. *Artificial Intelligence Review* **57**, 99 (2024).

6. Zhou B, Krähenbühl P, Koltun V. Does computer vision matter for action? *Science Robotics* **4**, eaaw6661 (2019).

7. He Y*, et al.* Deep learning based 3D segmentation in computer vision: A survey. *Information Fusion* **115**, 102722 (2025).

8. Lauriola I, Lavelli A, Aiolli F. An introduction to Deep Learning in Natural Language Processing: Models, techniques, and tools. *Neurocomputing* **470**, 443-456 (2022).

9. Sasidhar KN, Siboni NH, Mianroodi JR, Rohwerder M, Neugebauer J, Raabe D. Enhancing corrosion-resistant alloy design through natural language processing and deep learning. *Science Advances* **9**, eadg7992 (2023).

10. Hirschberg J, Manning CD. Advances in natural language processing. *Science* **349**, 261-266 (2015).

11. Khurana D, Koli A, Khatter K, Singh S. Natural language processing: state of the art, current trends and challenges. *Multimedia Tools and Applications* **82**, 3713-3744 (2023).

12. Tian Y, Ye Q, Doermann D. YOLOv12: Attention-Centric Real-Time Object Detectors. *arXiv e-prints*, arXiv:2502.12524 (2025).

13. Dosovitskiy A*, et al.* An Image is Worth 16x16 Words: Transformers for Image Recognition at Scale. In: *International Conference on Learning Representations*) (2021).

14. He K, Zhang X, Ren S, Sun J. Deep Residual Learning for Image Recognition. In: *2016 IEEE Conference on Computer Vision and Pattern Recognition (CVPR)*) (2016).

15. Touvron H*, et al.* LLaMA: Open and Efficient Foundation Language Models. *arXiv e-prints*, arXiv:2302.13971 (2023).

16. Vaswani A*, et al.* Attention is all you need. In: *Proceedings of the 31st International Conference on Neural Information Processing Systems*). Curran Associates Inc. (2017).

17. Li J, Li D, Xiong C, Hoi S. BLIP: Bootstrapping Language-Image Pre-training for Unified Vision-Language Understanding and Generation. *arXiv e-prints*, arXiv:2201.12086 (2022).

18. Yin S*, et al.* A survey on multimodal large language models. *National Science Review* **11**, nwae403 (2024).

19. Radford A*, et al.* Learning Transferable Visual Models From Natural Language Supervision. In: *Proceedings of the 38th International Conference on Machine Learning* (eds Marina M, Tong Z). PMLR (2021).

20. Zhang W*, et al.* Neuro-inspired computing chips. *Nature Electronics* **3**, 371-382 (2020).

21. Huo Q*, et al.* A computing-in-memory macro based on three-dimensional resistive random-access memory. *Nature Electronics* **5**, 469-477 (2022).

22. Rasch MJ*, et al.* Hardware-aware training for large-scale and diverse deep learning inference workloads using in-memory computing-based accelerators. *Nature Communications* **14**, 5282 (2023).

23. Joshi V*, et al.* Accurate deep neural network inference using computational phase-change memory. *Nature Communications* **11**, 2473 (2020).

24. Hassanpour M, Riera M, González A. A Survey of Near-Data Processing Architectures for Neural Networks (2022).

25. Yamashita R, Nishio M, Do RKG, Togashi K. Convolutional neural networks: an overview and application in radiology. *Insights into Imaging* **9**, 611-629 (2018).

26. Xu B, Wang N, Chen T, Li M. Empirical Evaluation of Rectified Activations in Convolutional Network. *arXiv e-prints*, arXiv:1505.00853 (2015).

27. Cao R*, et al.* Compact artificial neuron based on anti-ferroelectric transistor. *Nat Commun* **13**, 7018 (2022).

28. Gao J*, et al.* Reconfigurable neuromorphic functions in antiferroelectric transistors through coupled polarization switching and charge trapping dynamics. *Nat Commun* **16**, 4368 (2025).

29. Zhou G*, et al.* Full hardware implementation of neuromorphic visual system based on multimodal optoelectronic resistive memory arrays for versatile image processing. *Nature Communications* **14**, 8489 (2023).

30. Wan W*, et al.* A compute-in-memory chip based on resistive random-access memory. *Nature* **608**, 504-512 (2022).

31. Peng X, Huang S, Jiang H, Lu A, Yu S. DNN+NeuroSim V2.0: An End-to-End Benchmarking Framework for Compute-in-Memory Accelerators for On-Chip Training. *IEEE Transactions on Computer-Aided Design of Integrated Circuits and Systems* **40**, 2306-2319 (2021).

32. Yi T, Zhong-liang W, Guo-qiang N, Li-qiang T. NLOS single scattering model in digital UV communication. In: *Proc.SPIE*) (2008).

33. Krestinskaya O, Salama KN, James AP. Learning in Memristive Neural Network Architectures Using Analog Backpropagation Circuits. *IEEE Transactions on Circuits and Systems I: Regular Papers* **66**, 719-732 (2019).

34. Oh S*, et al.* Energy-efficient Mott activation neuron for full-hardware implementation of neural networks. *Nat Nanotechnol* **16**, 680-687 (2021).

35. Oh J*, et al.* Preventing Vanishing Gradient Problem of Hardware Neuromorphic System by Implementing Imidazole-Based Memristive ReLU Activation Neuron. *Adv Mater* **35**, e2300023 (2023).

36. Zou J*, et al.* An Artificial L-ReLU Neuron with Asymmetric Diffusive Memristor for High-Accuracy Neuromorphic Systems. *Advanced Functional Materials*, (2025).

37. Islam KM, Synowicki R, Ismael T, Oguntoye I, Grinalds N, Escarra MD. In-Plane and Out-of-Plane Optical Properties of Monolayer, Few-Layer, and Thin-Film MoS2 from 190 to 1700 nm and Their Application in Photonic Device Design. *Advanced Photonics Research* **2**, (2021).

38. He W, Kong L, Yu P, Yang G. Record-High Work-Function p-Type CuBiP(2) Se(6) Atomic Layers for High-Photoresponse van der Waals Vertical Heterostructure Phototransistor. *Adv Mater* **35**, e2209995 (2023).

39. Li H*, et al.* From Bulk to Monolayer MoS2: Evolution of Raman Scattering. *Advanced Functional Materials* **22**, 1385-1390 (2012).

40. Lee SY*, et al.* Large Work Function Modulation of Monolayer MoS2 by Ambient Gases. *ACS Nano* **10**, 6100-6107 (2016).

41. Lu C-P, Li G, Mao J, Wang L-M, Andrei EY. Bandgap, Mid-Gap States, and Gating Effects in MoS2. *Nano Letters* **14**, 4628-4633 (2014).

42. Chang T, Jo S-H, Lu W. Short-Term Memory to Long-Term Memory Transition in a Nanoscale Memristor. *ACS Nano* **5**, 7669-7676 (2011).

43. McGlynn SP. Concepts in Photoconductivity and Allied Problems. *Journal of the American Chemical Society* **86**, 5707-5707 (1964).

44. Yang J*, et al.* MedMNIST v2 - A large-scale lightweight benchmark for 2D and 3D biomedical image classification. *Scientific Data* **10**, 41 (2023).

45. Chattopadhay A, Sarkar A, Howlader P, Balasubramanian VN. Grad-CAM++: Generalized Gradient-Based Visual Explanations for Deep Convolutional Networks. In: *2018 IEEE Winter Conference on Applications of Computer Vision (WACV)*) (2018).

46. Krizhevsky A. Learning Multiple Layers of Features from Tiny Images. *University of Toronto*, (2009).

47. Parkhi OM, Vedaldi A, Zisserman A, Jawahar CV. Cats and dogs. In: *2012 IEEE Conference on Computer Vision and Pattern Recognition*) (2012).

48. Bossard L, Guillaumin M, Van Gool L. Food-101 – Mining Discriminative Components with Random Forests. In: *Computer Vision – ECCV 2014* (eds Fleet D, Pajdla T, Schiele B, Tuytelaars T). Springer International Publishing (2014).

49. Lecun Y, Bottou L, Bengio Y, Haffner P. Gradient-based learning applied to document recognition. *Proceedings of the IEEE* **86**, 2278-2324 (1998).

Acknowledgments
This work is supported by National Key Research and Development Program of China (Grant No. 2022YFA1405600), Beijing Natural Science Foundation (Grant No. Z210006) and Start-up Research Fund for Young Scholar of Beijing Institute of Technology. We acknowledge the support provided by the Analysis and Testing Center of Beijing Institute of Technology.

Author Contributions
Y.L. conceived the study, wrote the manuscript with input from all authors, and performed the experiments, analyses, and simulations. Z.W. and F.X. carried out the PFM measurements. D.Y., W.Z., and T.Y., contributed to the analysis of the experimental data and provided suggestions. The study was supervised by H.W. and L.S. All authors contributed to the discussion and revision of the manuscript.

Competing interests
The authors declare no competing interests.

Figure Legends/Captions

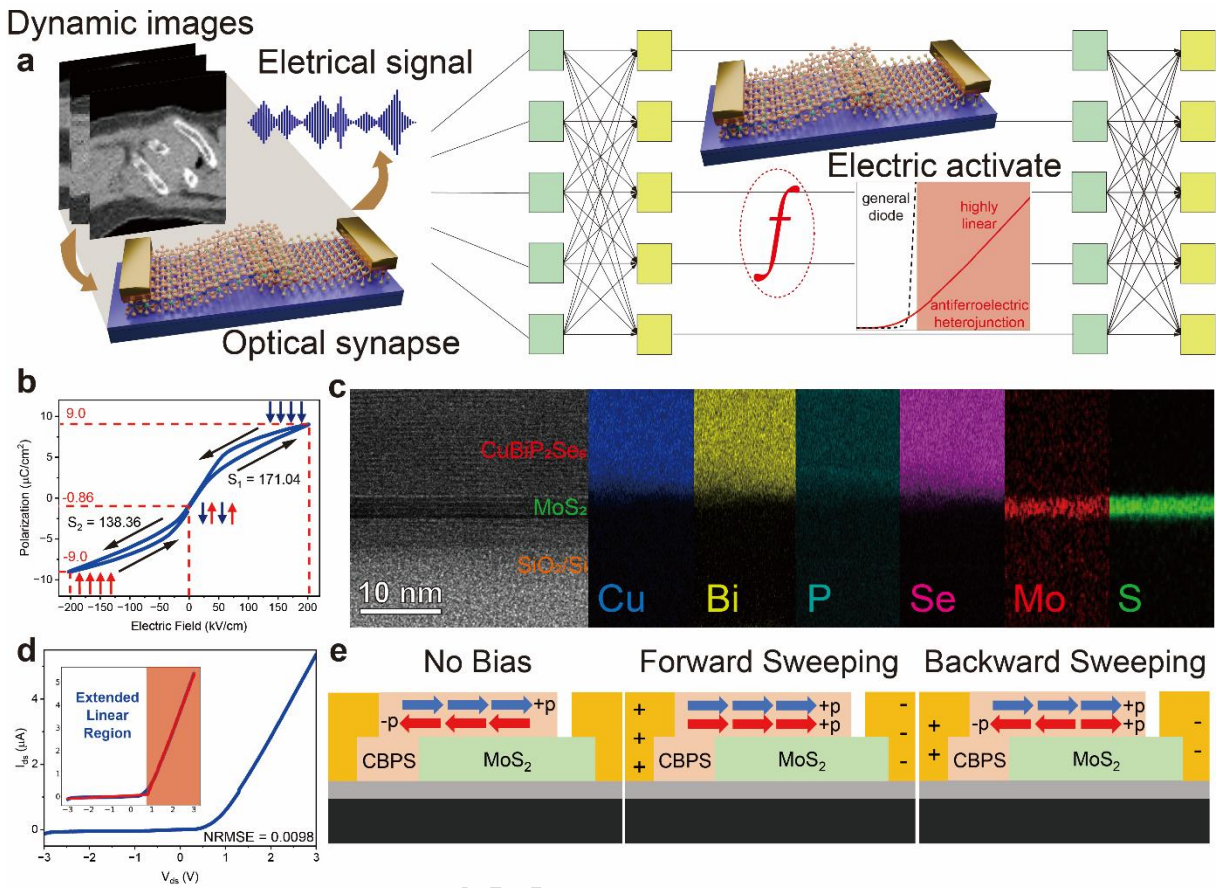

Figure 1. The schematic diagram of the in-sensor computing system and the characterization of the device. **a** Schematic diagram of a CBPS/MoS_2 heterojunction based in-sensor computing system, in which the heterojunction is applied as the activation of linear layers. **b** Polarization–electric hysteresis loops measured from CBPS antiferroelectric capacitor. The loop areas S_1 and S_2 obtained during forward and reverse scans are 171.04 and 138.36, respectively. **c** TEM image and the corresponding EDS mapping of the CBPS/MoS_2 heterostructure. **d** I-V output characteristics of the CBPS/MoS_2 heterojunction, measured with the scanning voltage V_{ds} sweep from -3 V to +3 V. **e** The mechanism of the heterostructure under voltage sweeping. In the initial state without bias, the ferroelectric domains are not flipped and persist in their opposite orientation. The application of a forward voltage sweeping initiates polarization switching of the domains. When the field polarity is reversed, the domains subsequently depolarize.

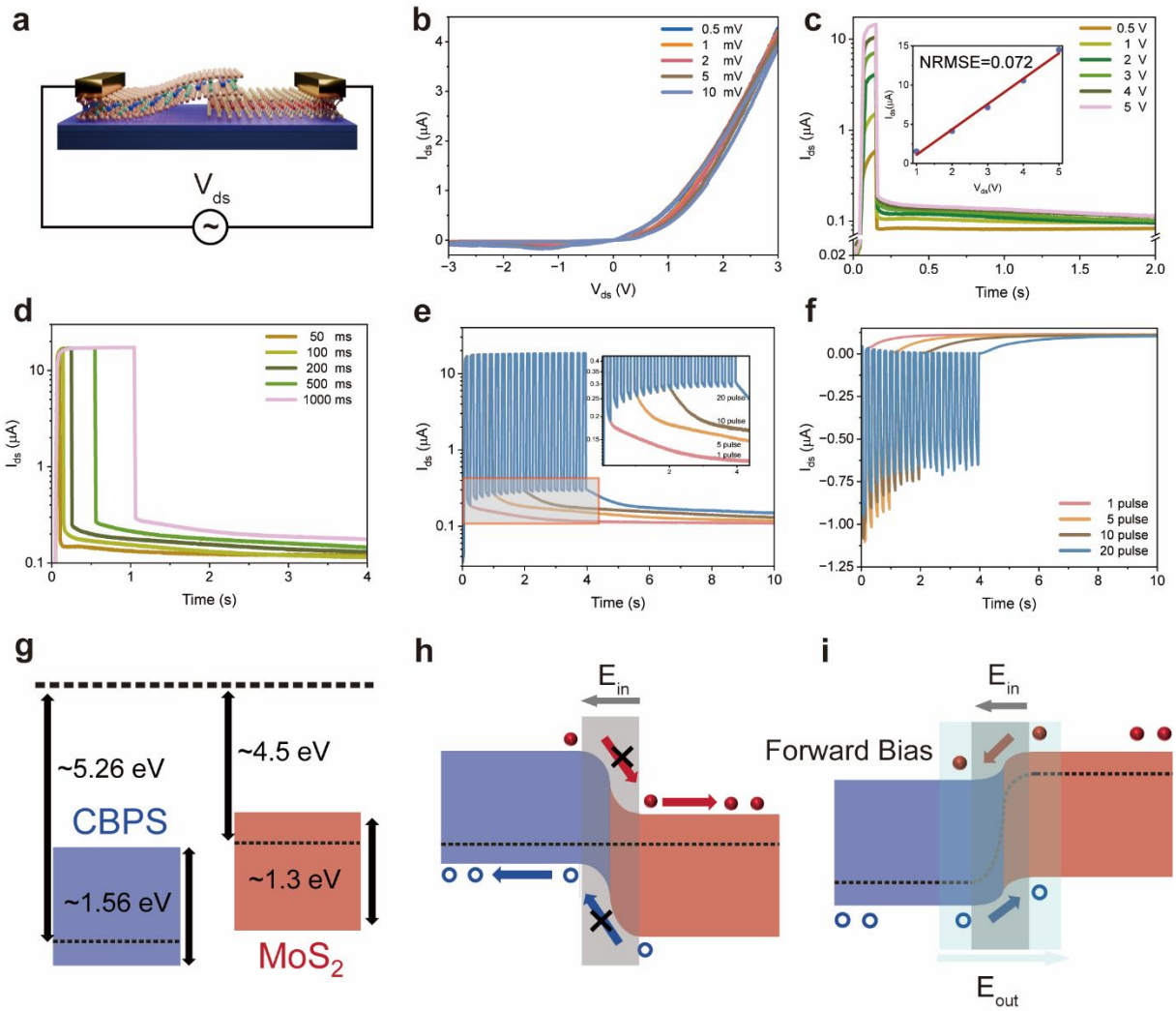

Figure 2. Electrical performance of the CBPS/MoS_2 heterojunction. **a** Schematic illustration of the CBPS/MoS_2 heterojunction structure, the left component is CBPS, and the right is MoS_2. A voltage V_d is applied to the CBPS terminal, while a voltage V_s is applied to the MoS_2 terminal. **b** Bidirectional I-V scan. No memory window is observed under reverse bias, while only a small memory window appears under forward bias. **c-e** Evolution of the channel conductance variation of the CBPS/MoS_2 heterojunction triggered by electrical pulses with (c, inset, The extraction of response signals under different electrical pulse amplitudes reveals a high degree of linearity between the response signals and the pulse amplitudes.) different pulse amplitude, (d) different pulse width (readout bias kept as 0.1 V) and, (e) different pulse number (pulse width, 100 ms, pulse interval, 100 ms). The inset in (e) is the magnified area of the red square. **f** Continuously applying negative electrical pulses with different amplitudes (pulse amplitude is -5 V). **g-i** The energy band alignment diagram of the CBPS and MoS_2 (g) before and (h) after contact. Diagrams of the energy band alignment of the CBPS/MoS_2 vdWs heterojunction under (i) forward bias.

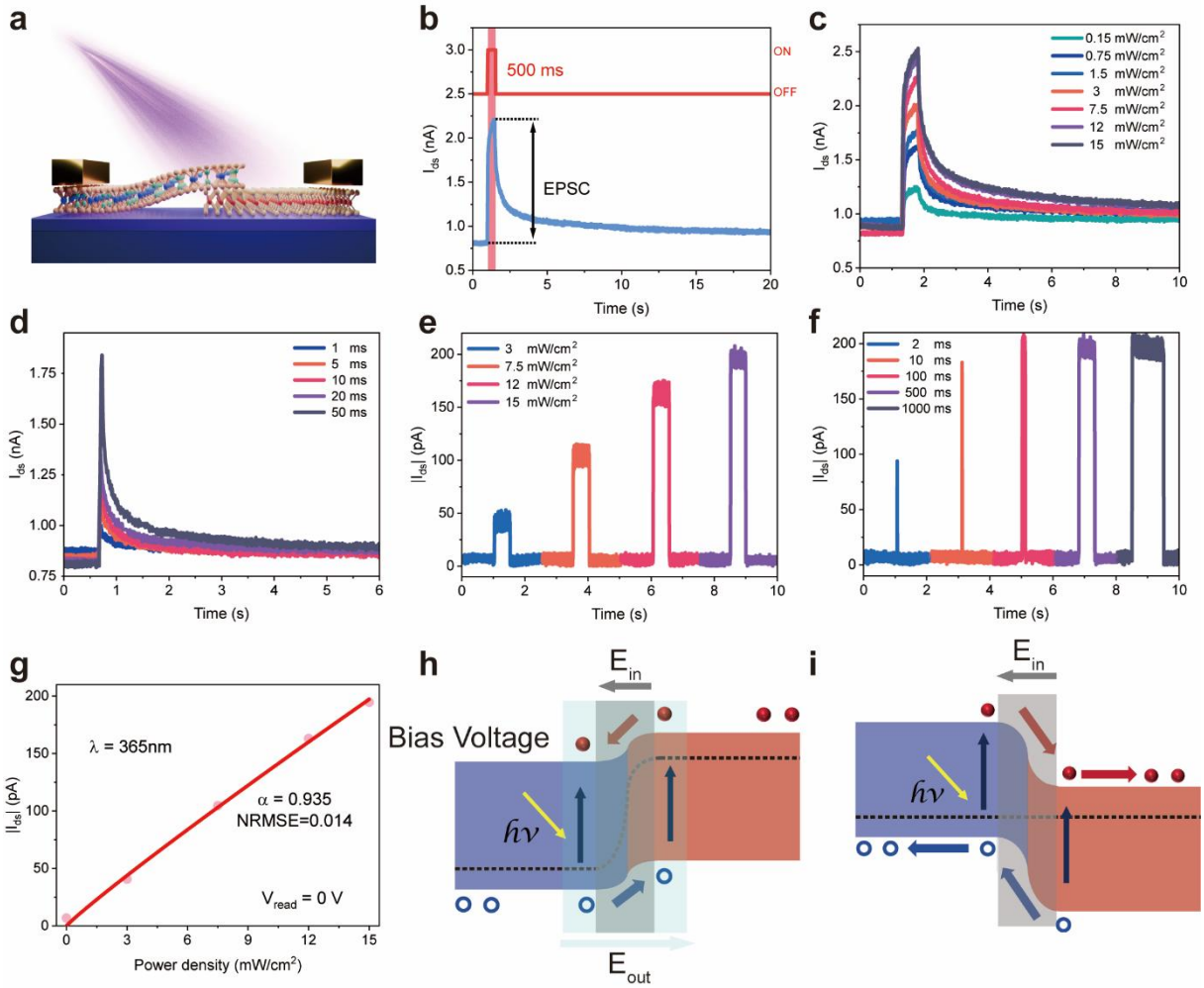

Figure 3. 365-nm laser pulse triggered memory behavior of the CBPS/MoS_2 heterojunction. **a** Schematic illustration of the CBPS/MoS_2 heterojunction under 365 nm illumination. **b** EPSC triggered by a 365 nm optical pulse (pulse width 500 ms). **c-d** 365 nm laser pulse triggered channel conductance variation under (c) different pulse width and (d) different power densities (readout bias kept as 0.1 V). **e-f** Photocurrent of CBPS/MoS_2 heterojunction under (e) different power density and (f) different pulse width at zero bias voltage. **g** The variation of photocurrent with light intensity under zero bias voltage. **h-i** Diagram of the energy band alignment of the CBPS/MoS_2 van der Waals heterojunction under illumination with (h) 0.1 V forward bias voltage and (i) zero bias voltage.

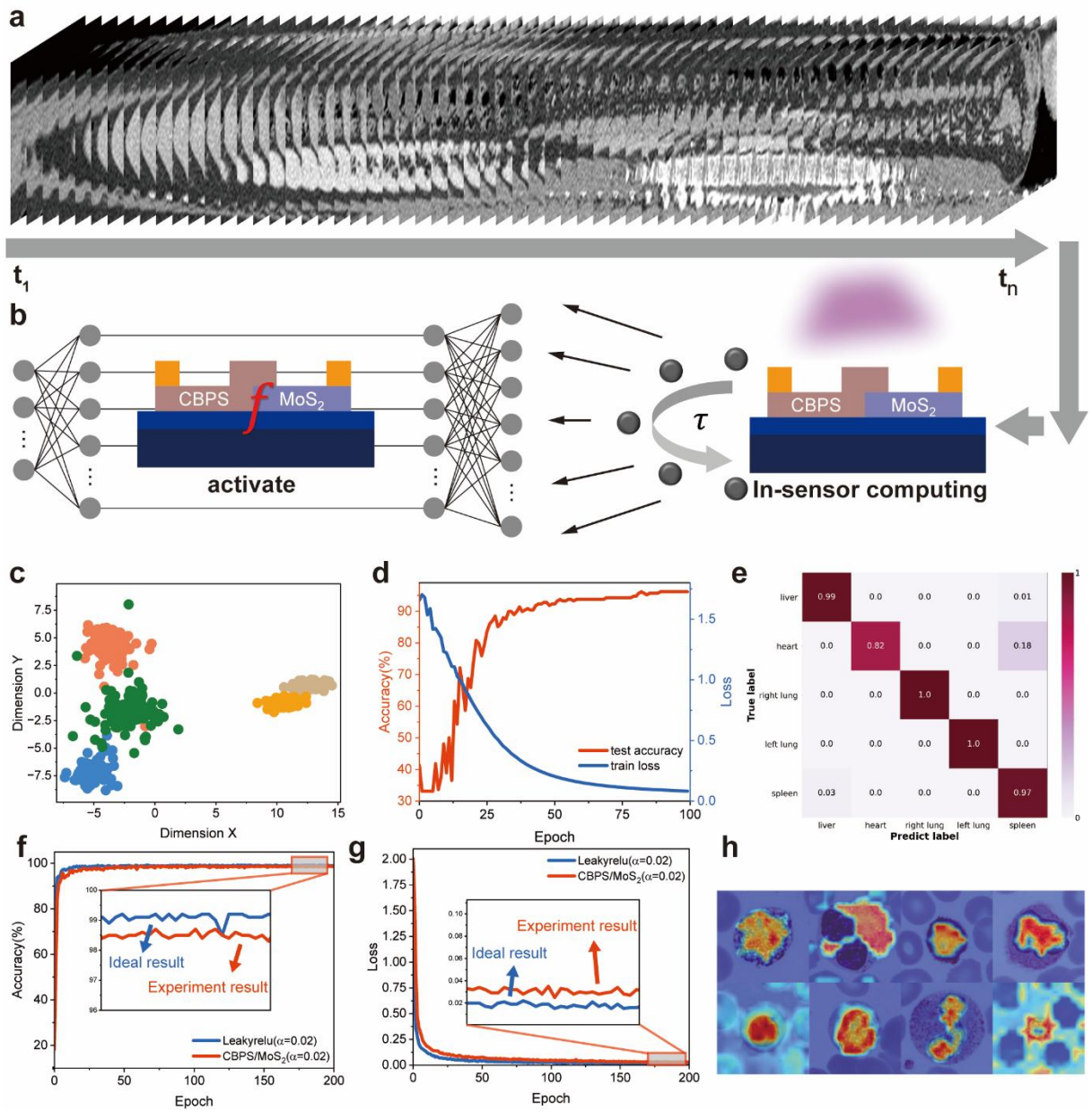

Figure 4 Dual functional CBPS/MoS_2 heterojunction based in-sensor computing for 3D medical image classification. **a-b** Schematic illustration of the neuromorphic computing system for classifying the OrganMNIST3D dataset. **a** 3D organ CT images decomposed frame by frame, with a total of 64 frames from t_1 to t_n. **b** Schematic diagram of the dual-functional heterojunction based in-sensor computing system. **c** Dimensionality reduction of heterojunction reservoir outputs using linear discriminant analysis (LDA). **d** Training process of the neural network based on heterojunction reservoir and activation function, where the red line represents the variation of test accuracy over training epochs, while the blue line denotes the change in training loss over epochs. **e** Confusion matrix on classifying the test set. **f-g** The (f) test accuracy and (g) training loss of vision transformer trained on the BloodMNIST dataset vary with the epochs. The blue line represents the ideal LeakyReLU activation function with α=0.02, while the red line represents the activation function derived from the physical properties of the CBPS/MoS_2 heterojunction.

Specifically, the ideal LeakyReLU achieved a peak accuracy of 99.2% with a minimum loss of 0.015, whereas the physical activation function resulted in only a 0.3% reduction in accuracy and a minimum loss of 0.025. **h** The heatmap obtained from gradient based visualization analysis of the image in (b) shows that the gradients mainly cover the most critical cellular regions.

Editor's summary:
The authors demonstrate a dual-functional antiferroelectric device that combines sensing, memory, and neural activation in a single architecture, enabling compact and low power in-sensor computing for medical image recognition.

Peer review information: *Nature Communications* thanks Minseong Park, Xianyue Zhao and the other anonymous reviewer(s) for their contribution to the peer review of this work. A peer review file is available.